

## Attosecond real-time observation of electron tunnelling and multi-electron dynamics in atoms - Supplementary Information -

M. Uiberacker,<sup>1,2,\*</sup> Th. Uphues,<sup>3,\*</sup> M. Schultze,<sup>2,\*</sup> A.J. Verhoef,<sup>2,4,\*</sup> V. Yakovlev,<sup>1</sup> M.F. Kling,<sup>5</sup>  
J. Rauschenberger,<sup>1,2</sup> N.M. Kabachnik,<sup>3,6</sup> H. Schröder,<sup>2</sup> M. Lezius,<sup>2</sup> K.L. Kompa,<sup>2</sup> H.-G. Müller,<sup>5</sup>  
M.J.J. Vrakking,<sup>5</sup> S. Hendel,<sup>3</sup> U. Kleineberg,<sup>1</sup> U. Heinzmann,<sup>3</sup> M. Drescher,<sup>7</sup> and F. Krausz<sup>1,2,4</sup>

<sup>1</sup>Department für Physik, Ludwig-Maximilians-Universität, Am Coulombwall 1, D-85748 Garching, Germany

<sup>2</sup>Max-Planck-Institut für Quantenoptik, Hans-Kopfermann-Str. 1, D-85748 Garching, Germany

<sup>3</sup>Fakultät für Physik, Universität Bielefeld, Universitätsstr. 25, D-33615 Bielefeld, Germany

<sup>4</sup>Institut für Photonik, Technische Universität Wien, Gusshausstrasse 27/387, A-1040 Vienna, Austria

<sup>5</sup>FOM-Instituut voor Atoom- en Molecuulfysica (AMOLF),

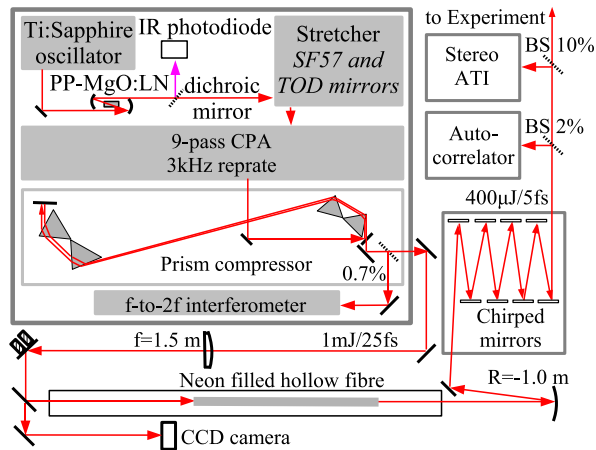
Kruislaan 407, 1098SJ Amsterdam, The Netherlands

<sup>6</sup>Institute of Nuclear Physics, Moscow State University, Moscow 119992, Russia

<sup>7</sup>Institut für Experimentalphysik, Universität Hamburg,

Luruper Chaussee 149, D-22671 Hamburg, Germany

### I. FEW-CYCLE, PHASE-CONTROLLED FEMTOSECOND LASER SYSTEM

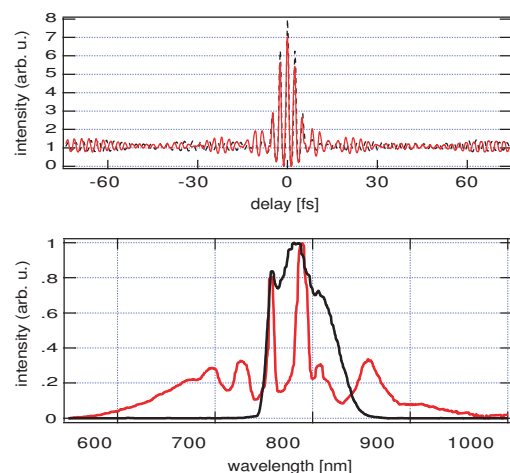


Suppl. Fig. 1: Schematic of the 3 kHz 5 fs laser system.

For this experiment we used a Ti:Sapphire laser system (Femtopower Compact Pro, Femtolasers), delivering 25-fs,  $\sim 1$ -mJ carrier-envelope-phase (CEP) stabilised pulses. A schematic of the laser setup is shown in Suppl. Fig. 1. The Ti:Sapphire oscillator delivers 6-fs pulses with 350 mW of average power at a repetition rate of 78 MHz. The pulses from the oscillator are focused into a periodically poled magnesium-oxide doped lithium niobate (PP-MgO:LN) crystal for spectral broadening and difference frequency generation (DFG) for phase stabilisation [1]. The pulses from the oscillator are stretched to 15 ps before being amplified to the millijoule level at a repetition rate of 3 kHz. Subsequent recompression yields bandwidth-limited pulses with a duration of  $\sim 25$  fs.

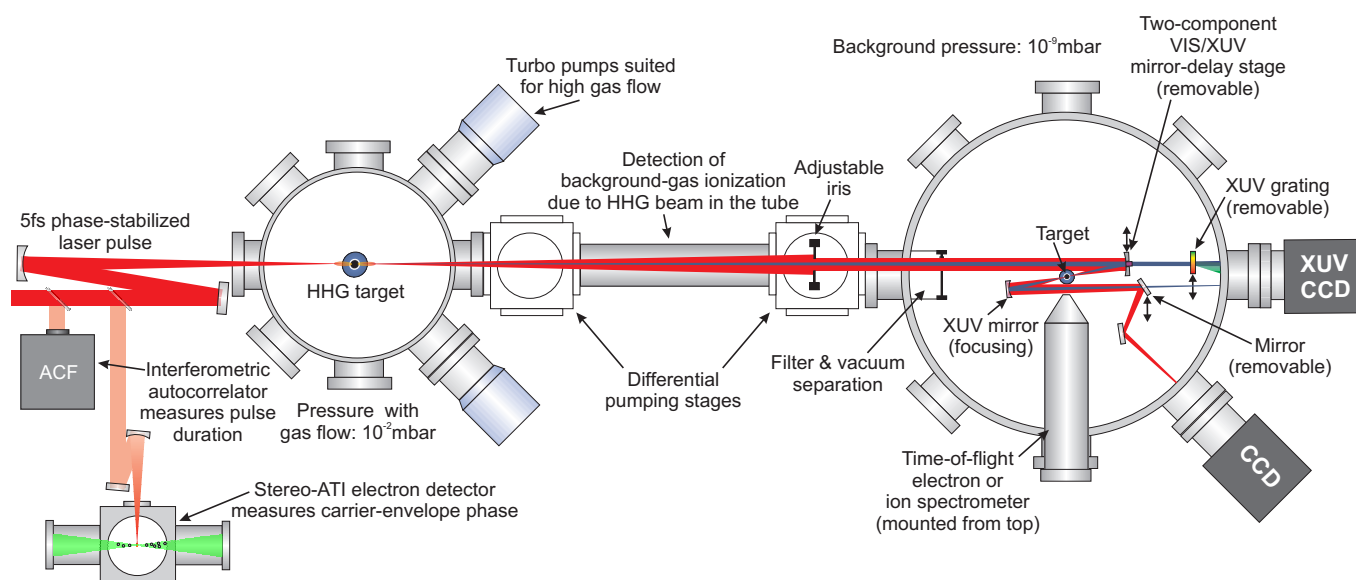
These pulses are focused into a hollow fibre filled with neon at approximately 2 bar for spectral broadening in order to be able to compress the pulses into the few-cycle regime. After the hollow fibre, the pulses are compressed with chirped mirrors, which are also used to (pre-)compensate for the dispersion introduced by air and glass components in the experiment. The pulse duration is monitored with a second order interferometric autocorrelator. Spectrum and autocorrelation of the compressed pulses are shown in Suppl. Fig. 2. The measured autocorrelation agrees very well with the calculated autocorrelation from the spectrum assuming a flat phase. The Fourier-limited pulse duration of the broadened spectrum after the hollow fibre is 4.8 fs. With this system we routinely generate pulses of 5-6 fs duration on a day-to-day basis.

An f-to-2f interferometer after the prism compressor is used to detect CEP drifts in the amplifier [2], which are compensated with a computer-controlled active feedback loop [3, 4]. The carrier-envelope phase can be monitored with a stereo-ATI phasemeter [5].



Suppl. Fig. 2: Top: second-order autocorrelation—measured (red) and calculated from the spectrum (black). Bottom: spectrum before (black) and after (red) the hollow fibre.

\*These authors contributed equally to this work



Suppl. Fig. 3: Schematic drawing of the vacuum, optical and diagnostic setup of the attosecond beamline.

## II. ATTOSECOND PUMP-PROBE SETUP

Here, we describe a newly developed attosecond beamline, which is based on the concept described in [6]. Main improvements of the original setup include strongly-reduced background pressure in the experimental chamber ( $\sim 10^{-8}$  mbar) and improved diagnostics. Furthermore, the accuracy and reproducibility of the delay between the attosecond-XUV and the NIR laser pulse has been significantly improved. Suppl. Fig. 3 shows the main layout of the system that was used in the present experiments. In what follows, we will describe essential parts of the system in more detail.

### A. High harmonic generation

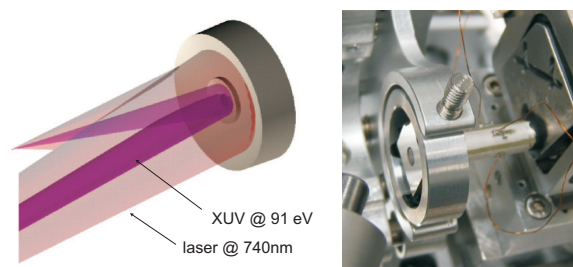
High harmonics of the NIR laser pulse are generated in a neon-filled tube of 2-mm diameter with a constant pressure (180–220 mbar). The pressure in the gas medium has been optimised for maximum conversion efficiency [7]. The resulting conversion efficiency for a photon energy of  $90\text{eV}$  is in the range of  $10^{-7}$  to  $10^{-8}$ . At a background neon pressure of  $\sim 10^{-2}$  mbar only some 2% of the generated 90-eV harmonics are reabsorbed in the HHG chamber before entering the first differential pumping stage (first cube in Suppl. Fig. 3).

### B. Differential pumping stages and ionization detector

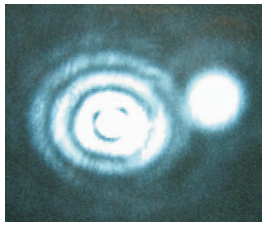
Two differential pumping stages are located between the HHG and the experimental chamber for further beam guiding and pumping to achieve UHV-conditions in the experimental chamber. The laser and the highly collimated

XUV beam emerging from the HHG source co-propagate collinearly over a distance of 2 m towards the double mirror assembly. The pressure gradient of 6–7 orders of magnitude under working conditions is achieved by the two differential pumping stages shown in Suppl. Fig. 3. The pressure is typically in the order of  $10^{-3}$  mbar in the first stage and  $10^{-6}$  mbar in the second stage (at the entrance to the experimental chamber).

An ionization detector between the two differential pumping stages of the beamline is used for monitoring the spectrally-integrated high-harmonic flux. The laser intensity can be adjusted with a motorised iris in the second cube shown in Suppl. Fig. 3. The relative laser intensity is measured with a silicon photodiode behind the gas target (not shown in Suppl. Fig. 3). The following filters may be inserted into the beam (Suppl. Fig. 3): (1) a  $2\text{-}\mu\text{m}$  pellicle to transmit only the NIR light and to adjust the temporal and spatial pulse overlap, (2) a  $1.5\text{-}\mu\text{m}$ -thick zirconium foil to transmit only the XUV light and monitor its beam shape and spectrum on a XUV-CCD camera, and (3) a  $150\text{ nm}$  thick,  $5\text{-mm}$ -diameter zirconium foil placed on a  $2\text{-}\mu\text{m}$ -thick nitrocellulose pellicle to prevent the NIR beam from hitting the inner part of the double mirror assembly in Suppl. Fig. 4.



Suppl. Fig. 4: Double mirror assembly.



Suppl. Fig. 5: Magnified image of the focus. Left  $\rightarrow$  outer mirror; right  $\rightarrow$  inner mirror; the focus of both mirrors is displaced for demonstration purposes.

### C. Experimental chamber

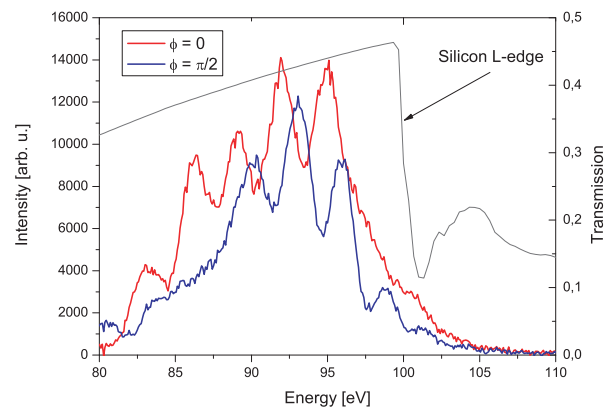
In the experimental chamber the background pressure is  $\sim 10^{-8}$  mbar. The Z-folded geometry (Suppl. Fig. 3) of the beam-path was chosen to accommodate various spectrometers (as e.g. the reflectron spectrometer used in this study [8–10]). The folding angle is kept below  $10^\circ$  to minimise astigmatism. A double-mirror assembly (see Suppl. Fig. 4) is used for focusing both the XUV and the NIR beam into the gas target under scrutiny. It consists of two identical Mo/Si multilayer mirrors ( $\lambda_0 \approx 91$  eV, bandwidth  $\approx 9$  eV), an outer mirror with a central hole of 5-mm diameter, incorporating one of a slightly smaller diameter (*inner mirror*). Both inner and outer mirror originate from the same substrate, ensuring identical radii of curvature ( $R = 245$  mm). The inner mirror is mounted on an ultra-high precision piezo translation stage, allowing alignment and translation with respect to the outer one. The two-component mirror assembly allows to control the delay between the laser and the XUV pulses with a maximum scanning range of 660 fs and a reproducibility of approximately 15 attoseconds.

In order to align the spatial and temporal overlap between the two beams the laser foci are imaged onto a CCD-camera (here filter (1) is used). Suppl. Fig. 5 shows an example image where the two foci are displaced.

The cut-off energy of the produced harmonic radiation can be adjusted such that it meets the energy range of highest reflectivity of the XUV mirror. For this purpose a grazing incidence flat-field grating (Hitachi) may be inserted into the XUV beam. Typical HHG spectra are shown in Suppl. Fig. 6.

### D. Determination of zero delay

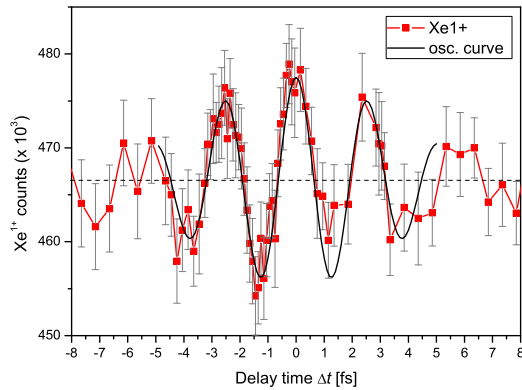
The delay time  $\Delta t = 0$  is defined as the overlap of the maxima of the envelopes of the XUV and the laser pulse. With the ion spectrometer currently used in our setup this time cannot be inferred directly. But it is possible to irradiate the inner and outer part of the double mirror setup with visible laser light only. Under these conditions a highly nonlinear autocorrelation of the above threshold ionization signal can be recorded. The ionization signal strongly depends on the constructive or destructive interference of the



Suppl. Fig. 6: Characteristic XUV spectra resolved for different CEO-phases. The cosine pulse ( $\phi=0$ ) generates a broad continuous spectrum in the cutoff-region, leading to a single attosecond pulse upon reflection on the Mo/Si-multilayer. The gray line shows the position of the silicon absorption edge that was used for the energy calibration.

two replica of the laser pulse and shows a pronounced maximum at perfect temporal overlap. From the high harmonic generation theory we know, that the most energetic attosecond burst (which will be selected by the bandpass filter) is shifted a quarter period behind the maximum of the XUV-light generating laser pulse. Taking this into account we can infer the zero delay between XUV and laser pulse. Fortunately the xenon measurements provide this information in the spectrum directly. A small fraction of the NIR beam leaks through the zirconium filter and is focused by the inner mirror together with the XUV beam into the gas target. Thus a modulation at around zero delay has been measured in the yield of  $\text{Xe}^{1+}$  and  $\text{Xe}^{2+}$ . The advantage of this method is the fact that the overlap position of the main laser pulse and the weak pulse leaking through the filter is recorded during the experiment. The different optical path lengths (main pulse penetrates through a pellicle foil) do not have to be considered. The data (red squares) in Suppl. Fig. 7 show the pronounced oscillations around zero delay. The solid curve is a cosine function with period of 2.55 fs and a Gaussian envelope centred at zero delay to show the perfect agreement with the laser period. The zero delay for the XUV/laser scans is shifted by a quarter period to the right in Suppl. Fig. 7. The data shown in Suppl. Fig. 7 have been recorded in an earlier measurement where we scanned accurately around zero delay. This was not the case in later scans. By fitting the temporal evolution of  $\text{Xe}^{4+}$  ions shown in this work with the evolution of  $\text{Xe}^{4+}$  ions in the calibration measurement we could determine zero delay with an accuracy of  $\pm 0.5$  fs.

Since the data have been recorded far from saturation, the ionization signal scales with the fourteenth or sixteenth power of the IR field amplitude. From this scaling and the modulation depth of the correlation signal depicted in Suppl. Fig. 7 we may conclude that the ratio of the field amplitude of the IR wave leaking through the zirconium filter and being reflected by the internal mirror to the field amplitude of the main IR wave reflected by the external



Suppl. Fig. 7: In-depth delay scan around zero delay.  $\text{Xe}^{1+}$  signal (red squares) shows pronounced oscillations. Black solid curve is a cosine function with 2.55 fs period with Gaussian envelope centred at  $\Delta t = 0$ .

mirror is a small fraction of 1%. This implies that this leakage has an influence of less than 1% on the Neon data of Fig. 4 in the paper, which have been recorded near saturation. Hence, this influence is buried in noise in the data. Compelling evidence for the negligible role of this leakage on the Neon data is provided by the lack of any significant modulation with a modulation period of  $T_L$  in the ionization signal measured in the absence of phase stabilization (thin grey line in Fig. 4a). Modulation of the ATI correlation signal in Suppl. Fig. 7 does not rely on carrier-envelope phase stabilization. Hence, if the leakage had any measurable influence of the  $\text{Ne}^{2+}$  ionization signal in Fig. 4, this modulation should show up in the thin grey curve in Fig. 4a, which is not the case.

### III. MODELLING THE ATTOSECOND TUNNELLING MEASUREMENT IN NEON

In order to get some basic understanding of our attosecond tunnelling measurements we used a simple model based on the assumptions that (i) the influence of the laser field on the interaction of the atom with the XUV pulse can be neglected and (ii) the laser ionization can be described by the non-adiabatic ionization theory of Yudin and Ivanov (YI theory) [12]. This modelling is especially useful in analysing the neon experiments, since it explains the nature of the observed “steps” and also clarifies what was measured in the experiment and what can be potentially measured using attosecond tunnelling.

In neon a few excited ionic states are populated by the XUV pulse in the presence of the strong NIR field. Let us denote the rate, with which the shake-up process populates the  $n$ -th excited ionic state by  $\chi_n(t)$ . Once populated at a time  $t$ , this state can be further ionized by the NIR field with the probability  $f_n(t)$ . The assumptions introduced above

allow us to write the probability of XUV excitation followed by laser ionization in the following general form:

$$p(\Delta t) = \sum_n \int_{-\infty}^{\infty} \chi_n(t + \Delta t) f_n(t) dt, \quad (1)$$

where  $\Delta t$  is the delay between the XUV and the laser pulses, and the summation is performed over all the  $\text{Ne}^{1+}$  states accessible to the NIR field. Choosing an appropriate intensity of the NIR field and an appropriate delay one may be able to make an attosecond tunnelling measurement for one single state  $n$ , but the measured quantity is always a correlation function, from which only one of the functions, either  $\chi(t)$  or  $f(t)$  can be reconstructed, provided that the other function is known. An important exception is the case, when the state is populated within such a short time that the probability of laser ionization can be neglected on this time scale. In this case  $\chi(t)$  can be approximated by a delta-function, and the measured probability of double ionization provides a direct time-resolved measurement of the laser ionization:  $p(\Delta t) = f(-\Delta t)$ .

Eq. (1) is no longer applicable if the NIR field significantly affects the shake-up probability. This is probably the origin of the small “dips” visible on Fig. 4 of the main paper. Since the magnitude of these dips is smaller than the error bars, we do not attempt to draw any conclusions from the presence of the dips, but we recognise that potentially they provide valuable information about the influence of an external field on the shake-up process and multi-electron dynamics of an atom in a strong laser field.

In order to determine how different excited  $\text{Ne}^{1+}$  states contribute to the measured signal, we modelled the laser ionization using the YI theory [12], which describes the sub-cycle strong-field ionization dynamics in both, the tunnelling and the multi-photon regimes, being especially useful in the intermediate regime  $\gamma \gtrsim 1$ . In contrast to the widely used ADK formula, this theory doesn't severely underestimate the ionization probability for small laser intensities, because it has a correct asymptotic behaviour in the multi-photon regime:  $\Gamma(t) \sim I_L^N$ , where  $\Gamma$  is the ionization rate,  $I_L$  is the laser intensity, and  $N$  is the number of photons required for ionization.

We also assume that the absorption of an XUV photon immediately populates the excited ionic states, so that  $\chi_n(t) = a_n I_X(t)$ . The relative values of the probabilities  $a_n$  can be inferred from the relative intensity of the corresponding photoelectron spectral lines detected in synchrotron measurements [11] and are listed as line intensities in Suppl. Table I. Using these models equation (1) can be written as

$$p(\Delta t) = \sum_n a_n \int_{-\infty}^{\infty} dt I_X(t + \Delta t) \left( 1 - e^{-\int_t^{\infty} dt' \Gamma_n(t')} \right), \quad (2)$$

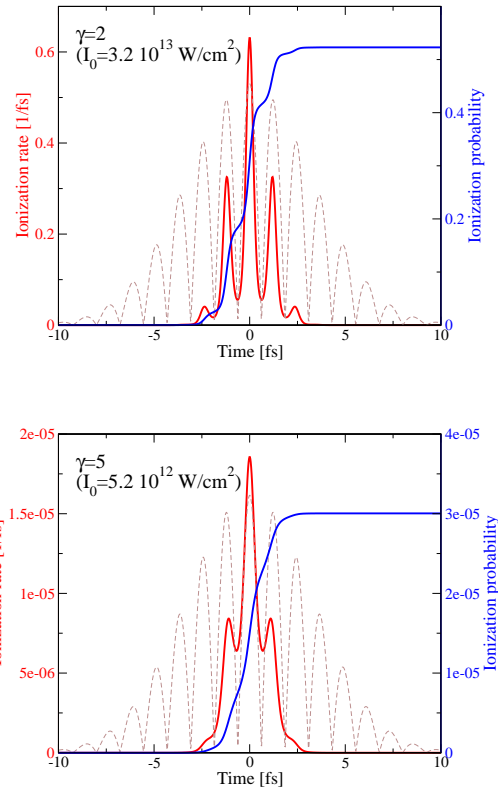
where  $\Gamma_n(t')$  is the rate of laser ionization from the  $n$ -th excited ionic state. The result of this simulation is shown in Fig. 4 of the main paper. The laser field was approximated by a 5.5-fs Gaussian pulse with a peak intensity of  $7 \cdot 10^{13} \text{ W/cm}^2$  and a central wavelength of 740 nm.

configuration	$W_b$ , eV	intensity of photoelectron spectral lines [arb. units]	barrier-suppression intensity [ $\text{W}/\text{cm}^2$ ]
$2s^2 2p^4 (^3P) 3s$	13.2	0.3	$3.0 \cdot 10^{13}$
$2s^2 2p^4 (^1D) 3s$	13.6	4.2	$3.4 \cdot 10^{13}$
$2s^2 2p^4 (^3P) 3p$	9.7	4.9	$8.9 \cdot 10^{12}$
$2s^2 2p^4 (^1D) 3p$	10.0	14.4	$1.0 \cdot 10^{13}$
$2s^2 2p^4 (^1S) 3s$	13.6	7.2	$3.4 \cdot 10^{13}$
$2s^2 2p^4 (^3P) 3d$	6.1	1.3	$1.4 \cdot 10^{12}$
$2s^2 2p^4 (^3P) 4s$	6.0	0.1	$1.3 \cdot 10^{12}$
$2s^2 2p^4 (^3P) 4p$	4.6	3.2	$4.3 \cdot 10^{11}$
$2s^2 2p^4 (^3P) 4d$	3.4	0.5	$1.3 \cdot 10^{11}$
$2s^2 2p^4 (^1S) 3p$	10.0	4.4	$9.9 \cdot 10^{12}$
$2s^2 2p^4 (^1D) 3d$	6.2	2.2	$1.4 \cdot 10^{12}$
$2s^2 2p^4 (^1D) 4p$	4.8	2.5	$5.4 \cdot 10^{11}$
$2s^2 2p^4 (^1S) 3d$	6.2	1.0	$1.5 \cdot 10^{12}$

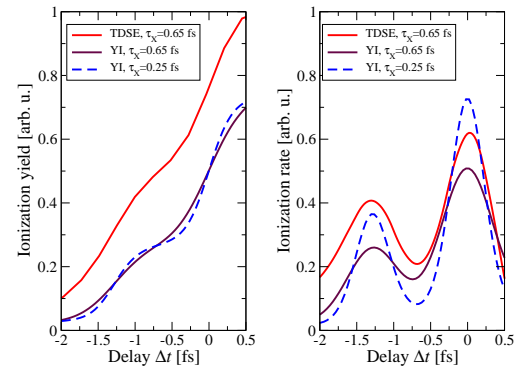
Suppl. Table I:  $\text{Ne}^{1+}$  states, based on [11], see text for details.

A closer look at the conditions, under which the “steps” appear in the simulations, reveals that for most of them the Keldysh parameter has a value between 2 and 3, i.e. the laser ionization occurs in the intermediate regime. The YI theory predicts that at these values of  $\gamma$  the ionization rate is still significantly modulated on the sub-cycle time scale. To demonstrate this we calculated the instantaneous rate and the time-integrated probability of strong-field ionization from a  $2s^2 2p^4 3s$  state of  $\text{Ne}^{1+}$  predicted by the YI theory (see Suppl. Fig. 8).

In order to verify the validity of the Yudin-Ivanov theory we carried out another simulation of the pump-probe experiment solving the time-dependent Schrödinger equation (TDSE) numerically in three spatial dimensions [14]. In these single-electron simulations the potential was adjusted to match the energies of the excited  $\text{Ne}^{1+}$  levels, and the central frequency of the XUV pulse was chosen to make selective photoexcitation to one of the levels. To provide the necessary spectral selectivity, a rather long, and hence relatively narrow-band 650-attosecond XUV pulse was used. Suppl. Fig. 9 presents results of a simulation, in which a  $2s^2 2p^4 3s$  state was excited by the XUV pulse and depleted by a 6.3-fs cosine-squared laser pulse with a central wavelength of 800 nm and a peak intensity of  $2.2 \cdot 10^{13} \text{ W}/\text{cm}^2$ . In spite of a large value of the Keldysh parameter ( $\gamma = 2.3$  at the peak of the pulse) and the fact that the XUV pulse was much longer than the one used in the experiment ( $\tau_X = 250$  attoseconds) the ionization yield exhibits sub-cycle behaviour. We also verified that the probability of ionizing a  $\text{Ne}^{1+}$  ion by a 6-fs laser pulse predicted by the Yudin-Ivanov theory agrees well with the TDSE simulations in the intensity range  $3 \cdot 10^{11} \text{ W}/\text{cm}^2$  ( $\gamma = 20$ ) and  $1.3 \cdot 10^{14} \text{ W}/\text{cm}^2$  ( $\gamma = 1$ ) confirming that the Yudin-Ivanov theory satisfactorily reproduces ionization rates in both the multi-photon and field ionization regime.



Suppl. Fig. 8: Strong-field ionization in the Yudin-Ivanov theory (see text).

Suppl. Fig. 9: Comparison of the Yudin-Ivanov theory with the exact 3D solution of the TDSE. The left panel shows the ionization yield  $p(\tau)$  as a function of the delay. The derivative  $p'(\tau)$ , which approximates the rate of the laser ionization, is shown on the right panel.

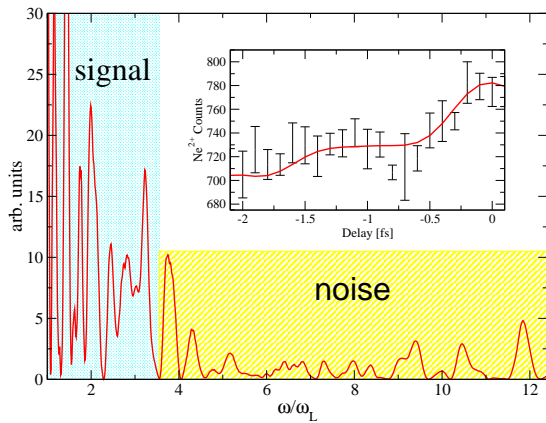
#### IV. DATA ANALYSIS

##### A. Rise time of the steps in the $\text{Ne}^{2+}$ signal

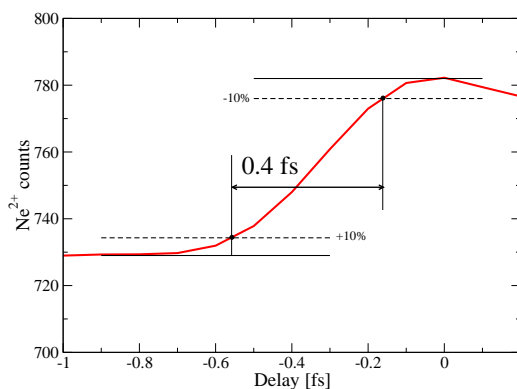
The fact that the probability of double ionization has the step-like dependency on the delay tells us that all the in-

volved processes must happen on a subfemtosecond time scale. Indeed, neither the time during which the shake-up state is populated, nor the time during which the tunnelling ionization channel is open can exceed the rise time of observed steps. In order to place an upper limit on these times the noise, with which the data were measured, must be taken into consideration.

In Suppl. Fig. 10 the power spectrum of the signal is plotted versus frequency normalised to the central frequency of the laser pulse. The fact that the steps occur two times per laser period is manifested by the peak at  $\omega = 2\omega_L$ . The part of the spectrum at high frequencies is dominated by noise. Suppressing those spectral components we filter the noise out of our data and simultaneously make the steps less steep. In general, it is not possible to precisely separate signal from noise, but we believe that by suppressing all spectral components larger than  $3.5\omega_L$  we place a reasonable upper limit on the step rise time.

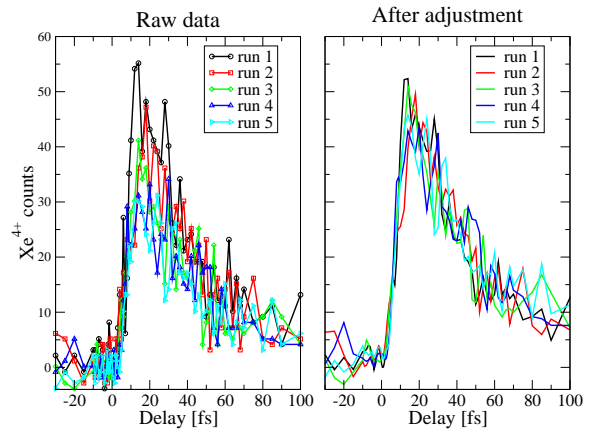


Suppl. Fig. 10: Noise suppression in the  $\text{Ne}^{2+}$  signal. The inset shows the original data and the filtered signal.



Suppl. Fig. 11: Determination of the step rise time.

The procedure that we used to quantify the step rise time is illustrated in Suppl. Fig. 11. First, we determine the values of the signal before and after a step. After that we



Suppl. Fig. 12: Adjustment of individual runs of the  $\text{Xe}^{4+}$  data.

are searching for the delays, at which the relative change of the signal amounts to 10%. The interval between these delays is defined as the rise time of the step. For different steps this value varies from 300 to 400 attoseconds.

## B. Error bars

In order to estimate the accuracy of the measurement and to minimise the impact of slow drift of different parameters the data were collected in several runs by scanning the delay from its minimal to its maximal value a few times. After that the data  $y_n(\Delta t)$  obtained in runs 2, 3, etc. were scaled and shifted in order to minimise the discrepancy with run 1 (see Suppl. Fig. 12 for the  $\text{Xe}^{4+}$  data as an example):

$$y_n^{\text{new}}(\Delta t) = ay(\Delta t) + b, \quad (3)$$

$$\sum_i |y_n^{\text{new}}(\Delta t_i) - y_1(\Delta t_i)|^2 \rightarrow \min. \quad (4)$$

After this adjustment the runs were averaged and the standard error was calculated for each delay. The lengths of the error bars in Figures 4 and 6 of the main paper are equal to twice the standard error.

## C. Fitting the temporal profiles

The temporal profiles are fitted with model functions that result from a convolution of a Gaussian representing the width of the NIR laser pulse with

$$A(t) = A_1 \left[ 1 - \exp\left(-\frac{\Delta t - \Delta t_0}{\tau_{A1}}\right) \right] \quad (5)$$

for the evolution of the  $\text{Xe}^{3+}$  ion yield and with

$$B(t) = B_1 \left[ \exp\left(-\frac{\Delta t - \Delta t_0}{\tau_{A1}}\right) - \exp\left(-\frac{\Delta t - \Delta t_0}{\tau_{A2}}\right) \right] \quad (6)$$

for the evolution of the  $\text{Xe}^{4+}$  ion yield, where  $\tau_{A1}$ ,  $\tau_{A2}$ , and  $t_0$  are fit parameters.

The weighted fits to the data are optimised by a program based on the Levenberg-Marquardt algorithm as im-

plemented in the Curve Fitting Toolbox 1.2 in Matlab R14 [13]. Errors in given time constants represent 95% confidence intervals.

- 
- [1] T. Fuji *et al.*, *Opt. Lett.* **30**, 332 (2005).  
[2] J. Rauschenberger, *et al.*, *Laser Phys. Lett.*, **3**, 37 (2006).  
[3] A. Baltuška, *et al.*, *IEEE J. QE.*, **9**, 972 (2003).  
[4] A. Baltuška, *et al.*, *Nature*, **421**, 611 (2003).  
[5] A. J. Verhoef, *et al.*, *Opt. Lett.*, submitted.  
[6] M. Drescher *et al.*, *Science* **291**, 1923 (2001).  
[7] M. Schnürer *et al.*, *Appl. Phys. B* **70**, 227 (2000).  
[8] H. Schröder, M. Wagner, S. Kaesdorf, K.L. Kompa, *Ber. Bunsenges. Phys. Chem.* **97**, 1688 (1993).  
[9] M. Wagner, H. Schröder, *Int. J. Mass Spect. Ion. Proc.* **128**, 31 (1993).  
[10] B. Witzel, H. Schröder, S. Kaesdorf, K.L. Kompa, *Int. J. Mass Spect. Ion. Proc.* **172**, 229 (1998).  
[11] A. Kikas, *et al.*, *J. El. Spectr. Rel. Phen.*, **77**, 241 (1996).  
[12] G.L. Yudin, M.Y. Ivanov, *Phys. Rev. A*, **64**, 013409 (2001).  
[13] J. Zerbs, Dissertation, Universität Göttingen (2005).  
[14] H.G. Muller, *Laser Physics*, **9**, 138-148 (1999).